Data Bank accession numbers

The atomic coordinates and structure factors of Cnx1G (1uux) and Ser583Ala (1uuy) have been deposited in the PDB.

Received 11 March; accepted 18 May 2004; doi:10.1038/nature02681.

1. Hille, R. The mononuclear molybdenum enzymes. *Chem. Rev.* **96,** 2757–2816 (1996).
2. Romao, M. J. *et al.* Crystal structure of the xanthine oxidase-related aldehyde oxido- reductase from *D. gigas. Science* **270,** 1170–1176 (1995).
3. Chan, M. K., Mukund, S., Kletzin, A., Adams, M. W. W. & Rees, D. C. Structure of a hyperthermophilic tungstopterin, aldehyde ferredoxin oxidoreductase. *Science* **267,** 1463–1469 (1995).
4. Mendel, R. R. & Schwarz, G. Biosynthesis and molecular biology of the molybdenum cofactor (Moco). *Met. Ions Biol. Syst.* **39,** 317–368 (2002).
5. Stiefel, E. I. Molybdenum bolsters the bioinorganic brigade. *Science* **272,** 1599–1600 (1996).
6. Enemark, J. H. & Cosper, M. M. Molybdenum enzymes and sulfur metabolism. *Met. Ions Biol. Syst.* **39,** 621–654 (2002).
7. Mendel, R. R. & Schwarz, G. Molybdoenzymes and molybdenum cofactor in plants. *Crit. Rev. Plant. Sci.* **18,** 33–69 (1999).
8. Johnson, J. L. *et al.* Inborn errors of molybdenum metabolism: combined deficiencies of sulfite oxidase and xanthine dehydrogenase in a patient lacking the molybdenum cofactor. *Proc. Natl Acad. Sci. USA* **77,** 3715–3719 (1980).
9. Shih, V. E. *et al.* Sulfite oxidase deficiency. Biochemical and clinical investigations of a hereditary metabolic disorder in sulfur metabolism. *N. Engl. J. Med.* **297,** 1022–1028 (1977).
10. Kuper, J., Winking, J., Hecht, H. J., Mendel, R. R. & Schwarz, G. The active site of the molybdenum cofactor biosynthetic protein domain Cnx1G. *Arch. Biochem. Biophys.* **411,** 36–46 (2003).
11. Schwarz, G. *et al.* The molybdenum cofactor biosynthetic protein Cnx1 complements molybdate-repairable mutants, transfers molybdenum to the metal binding pterin, and is associated with the cytoskeleton. *Plant Cell* **12,** 2455–2472 (2000).
12. Kuper, J. *et al. In vivo* detection of molybdate-binding proteins using a competition assay with ModE in *Escherichia coli*. *FEMS Microbiol. Lett.* **218,** 187–193 (2003).
13. Kisker, C. *et al.* Molecular basis of sulfite oxidase deficiency from the structure of sulfite oxidase. *Cell* **91,** 973–983 (1997).
14. Kuper, J., Palmer, T., Mendel, R. R. & Schwarz, G. Mutations in the molybdenum cofactor biosynthetic protein Cnx1G from *Arabidopsis thaliana* define functions for molybdopterin bind, Mo-insertion and molybdenum cofactor stabilization. *Proc. Natl Acad. Sci. USA* **97,** 6475–6480 (2000).
15. Lake, M. W., Wuebbens, M. M., Rajagopalan, K. V. & Schindelin, H. Mechanism of ubiquitin activation revealed by the structure of a bacterial MoeB–MoaD complex. *Nature* **414,** 325–329 (2001).
16. Schindelin, H., Kisker, C., Hilton, J., Rajagopalan, K. V. & Rees, D. C. Crystal structure of DMSO reductase: redox-linked changes in molybdopterin coordination. *Science* **272,** 1615–1621 (1996).
17. Schrader, N. *et al.* The crystal structure of plant sulfite oxidase provides insights into sulfite oxidation in plants and animals. *Structure* **11,** 1251–1263 (2003).
18. Santamaria-Araujo, J. A. *et al.* The tetrahydropyranopterin structure of the sulfur-free and metal-free molybdenum cofactor precursor. *J. Biol. Chem.* **279,** 15994–15999 (2004).
19. Bertero, M. G. *et al.* Insights into the respiratory electron transfer pathway from the structure of nitrate reductase A. *Nature Struct. Biol.* **10,** 681–687 (2003).
20. Nason, A. *et al. In vitro* formation of assimilatory reduced nicotinamide adenine dinucleotide phosphate: nitrate reductase from a Neurospora mutant and a component of molybdenum-enzymes. *Proc. Natl Acad. Sci. USA* **68,** 3242–3246 (1971).
21. Xiang, S., Nichols, J., Rajagopalan, K. V. & Schindelin, H. The crystal structure of *Escherichia coli* MoeA and its relationship to the multifunctional protein Gephyrin. *Structure* **9,** 299–310 (2001).
22. Schrag, J. D. *et al.* The crystal structure of *Escherichia coli* MoeA, a protein from the molybdopterin synthesis pathway. *J. Mol. Biol.* **310,** 419–431 (2001).
23. Moorhead, G. B. *et al.* Purification of a plant nucleotide pyrophosphatase as a protein that interferes with nitrate reductase and glutamine synthetase assays. *Eur. J. Biochem.* **270,** 1356–1362 (2003).
24. Mercer, J. F. The molecular basis of copper-transport diseases. *Trends Mol. Med.* **7,** 64–69 (2001).
25. Mason, J. Thiomolybdates: mediators of molybdenum toxicity and enzyme inhibitors. *Toxicology* **42,** 99–109 (1986).
26. Navaza, J. AMORE—an automated package for molecular replacement. *Acta Crystallogr. A* **50,** 157–163 (1994).
27. Jones, T. A., Zou, J. Y., Cowan, S. W. & Kjeldgaard, M. Improved methods for building protein models in electron density maps and the location of errors in these models. *Acta Crystallogr. A* **47,** 110–119 (1991).
28. Murshudov, G., Vagin, A. & Dodson, E. Refinement of macromolecular structures by the maximum likelihood method. *Acta Crystallogr. D* **53,** 240–255 (1997).
29. Guse, A. *et al.* Biochemical and structural analysis of the molybdenum cofactor biosynthesis protein MobA. *J. Biol. Chem.* **278,** 25302–25307 (2003).
30. Nicholls, A., Sharp, K. A. & Honig, B. Protein folding and association: insights from the interfacial and thermodynamic properties of hydrocarbons. *Proteins Struct. Funct. Genet.* **11,** 281–296 (1991).

Supplementary Information accompanies the paper on **www.nature.com/nature**.

Acknowledgements We thank R. N. Pau for inspiring discussion; T. Otte and F. Koenig for technical assistance; the staff at beamlines BW6 at DESY and PSF-BL2 at BESSY; and V. Wray for critically reading the manuscript. This work was supported by grants from the Deutsche Forschungsgemeinschaft (to H.J.H., R.R.M. and G.S.), and the Fonds der Chemischen Industrie and the Fritz Thyssen Stiftung (to R.R.M.).

Competing interests statement The authors declare that they have no competing financial interests.

Correspondence and requests for materials should be addressed to G.S. (g.schwarz@tu-bs.de).

Electron microscopic analysis of KvAP voltage-dependent K^+ channels in an open conformation

Qiu-Xing Jiang[1], Da-Neng Wang[2] & Roderick MacKinnon[1]

[1]*Howard Hughes Medical Institute and Laboratory of Molecular Neurobiology and Biophysics, Rockefeller University, 1230 York Avenue, New York, New York 10021,USA*
[2]*Skirball Institute of Biomolecular Medicine, New York University Medical Center, 540 First Avenue, New York, New York 10016,USA*

Voltage-dependent ion channels serve as field-effect transistors by opening a gate in response to membrane voltage changes[1]. The gate's response to voltage is mediated by voltage sensors[2], which are arginine-containing structures that must move with respect to the membrane electric field. We have analysed by electron microscopy a voltage-dependent K^+ channel from *Aeropyrum pernix* (KvAP)[3]. Fab fragments were attached to 'voltage sensor paddles' and identified in the electron microscopy map at 10.5 Å resolution. The extracellular surface location of the Fab fragments in the map is consistent with the membrane-depolarized, open conformation of the channel in electrophysiological experiments. Comparison of the map with a crystal structure[4] demonstrates that the voltage sensor paddles are 'up' (that is, near the channel's extracellular surface) and situated at the protein–lipid interface. This finding supports the hypothesis that in response to changes in voltage the sensors move at the protein–lipid interface[5] rather than in a gating pore surrounded by protein[6,7].

Voltage-dependent cation channels have voltage sensors that contain a hydrophobic α-helix with arginine residues known as S4[1,2]. The movement of the cationic arginine residues relative to the membrane electric field energetically couples the pore conformation to transmembrane voltage[1,2]. How does such a movement occur? The crystal structure of a voltage-dependent K^+ channel KvAP showed that in each subunit S4 forms part of a helix-turn-helix structure termed a voltage sensor paddle[4]. In the crystal the paddles, which are attached to the pore by flexible hinges, are in an apparently non-native conformation (at the intracellular surface), probably owing to crystal packing constraints and the absence of a membrane. Despite uncertainties in the relationship between the KvAP crystal structure and its possible conformations in the membrane, the crystal structure conveyed a very interesting idea: that the voltage sensor paddles probably move relative to the pore for it to open. Experiments with biotin and avidin have lent strong support for this idea[5]. The voltage sensor paddles were hypothesized to move within the membrane at the protein–lipid interface. A more complete understanding of voltage-dependent gating, however, requires additional experiments, especially new protein structures under a variety of conditions.

We performed single particle reconstruction[8] from electron microscopy images of purified KvAP protein to obtain a three dimensional (3D) structure of the channel. In this method the channel is not subject to crystal packing forces. We attached four 33H1 Fab fragments, one to each voltage sensor, with three intentions. First, the mass of one KvAP tetramer is ~100 kDa, which is too small for accurate cryo-electron microscopy analysis[9]. Four Fab fragments increase the total particle mass to ~300 kDa, large enough for accurate single particle alignment. Second, the 33H1 Fab fragment binds to the voltage sensor in electrophysiological experiments only when the channel opens, and only from the extracellular side of the membrane (Fig. 1a)[5]. Therefore, we can assess whether the Fab positions are consistent with the electrophysiological experiments. Third, a crystal structure of the 33H1

Fab bound to the voltage sensor defines (at 1.9 Å resolution) the precise location of the voltage sensor paddle, which is fixed with respect to the Fab fragment (Fig. 1b)[4]. Therefore, by identifying the Fab fragments in the map we can infer the locations of the voltage sensor paddles.

An initial model was generated from images of single particles stained with ammonium molybdate (Fig. 1c and see Methods). This initial model was used as a starting point for analysis of cryo-negatively stained images (Fig. 1d). The use of negative stain in vitrified ice has been shown to increase the contrast of single particles[10], and limits the resolution[11] to the size of the stain molecules (~8.5 Å). Sufficient contrast allowed interactive particle picking and reliable alignment for single particle reconstruction (Fig. 1d). A 3D map was generated from ~21,400 particles (Fig. 1e). The resolution was estimated to be 10.5 Å based on a 0.5 threshold in the Fourier shell correlation (FSC, Fig. 1f)[12,13]. As expected at this resolution, many surface features are easily discernable, including α-helices projecting from the channel surface (Fig. 2a), two identifiable immunoglobulin domains for each Fab (Fig. 1e) and a groove separating the main β sheets within the variable immunoglobulin domain (Fig. 2e). Heterogeneity in the position of the constant domain with respect to the variable domain is evident in the map, as has been described in other electron microscope reconstructions with Fab fragments[14]. These features confirm that the map contains the structural details consistent with the estimation of resolution by FSC of 0.5, which has been shown to be a conservative definition of resolution[15].

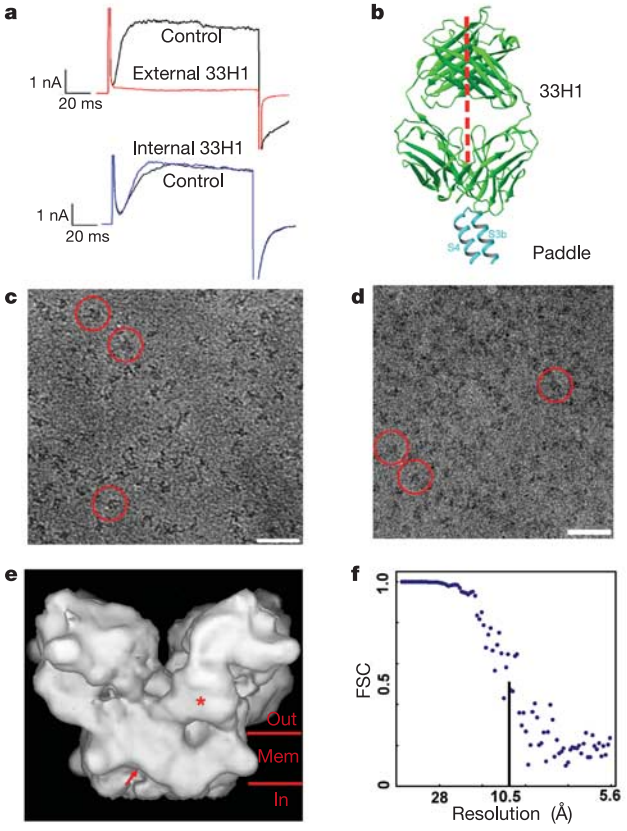

Figure 1 Structure of the KvAP–33H1 complex at 10.5 Å. **a**, Functional effect of the 33H1 Fab on the ionic current carried by KvAP channels in planar membranes. Depolarization to +100 mV elicited an outward K^+ current (black traces). Fab 33H1 inhibited ionic current from the extracellular side (red trace), but not from the intracellular side (blue trace). **b**, Structure of the 33H1 Fab fragment bound to the voltage sensor paddle as determined by X-ray crystallography[4] (PDB code 1ORS). The paddle is rigidly attached to the Fab fragment. The red dashed line represents the pseudo two-fold axis of the Fab fragment. **c**, Image of negatively stained KvAP–33H1 complexes. Protein appears black here and in **d**. Three particles are marked with red circles. The scale bar is 50 nm. **d**, Image of cryo-negatively stained KvAP–33H1 complexes. Select particles are marked with red circles. The particles were well separated and took different orientations. The scale bar is 50 nm. **e**, 3D map of the KvAP–33H1 complex at 10.5 Å. The red arrow identifies a position considered in Fig. 4a and b. The red asterisk marks the variable immunoglobulin domain and area shown in Fig. 2d. **f**, Fourier shell correlation (FSC) for the 3D map of the KvAP–33H1 complex from two maps calculated using two halves of the data. The 0.5 threshold corresponds to 10.5 Å.

To constrain the voltage sensor paddle with respect to the pore we docked the crystal structures of the pore and the Fab–paddle into the map independently. The pore from the KvAP crystal structure[4] fits well without modification, with the S6 (inner) helices, inserting into helical tubes projecting from the intracellular surface of the map (Fig. 2b). The recognizable chirality of this structure defines unambiguously the handedness of the map. On the extracellular side, the level of the selectivity filter opening and turret structures conform to the map's surface (Fig. 2c). The position of the pore is therefore accurately defined with respect to rotation and translation.

The constant immunoglobulin domain of Fab and the variable domain of Fab, coupled to the voltage sensor paddle, were docked separately. The constant domain was not very well constrained because of its apparent intrinsic mobility in the particles. But the variable domain, which is attached directly to the voltage sensor paddle, conforms very well both to the volume and surface features of the map, allowing its accurate placement (Fig. 2d, e), with a single ambiguity. A Fab fragment has a pseudo two-fold axis parallel to its longest dimension (Fig. 1b), and therefore at 10.5 Å resolution there are two (but only two) possible ways related by 180° rotation to place the Fab fragment into the map. These two ways define two possible orientations of the voltage sensor paddle with respect to the pore, because the paddle is fixed relative to the Fab fragment (Fig. 1b). These are shown, as viewed from the side (Fig. 3a, b) and in cross-section near the level of the extracellular surface (Fig. 3c, d).

The location of density for the Fab fragments at the channel's extracellular surface in the map (Figs 1e and 2c) is consistent with electrophysiological studies showing that 33H1 Fabs bind only from the extracellular side and only when a channel opens (Fig. 1a)[5]. This correlation between structure and activity of the Fabs in electrophysiological experiments leads us to conclude that the voltage sensors are in an open conformation.

In either of the two possible orientations, the voltage sensor paddles are located at the lateral (membrane-facing) edge of the map, at the channel's outer perimeter with an entire face of S4 exposed to what would be the membrane in the native state (Fig. 3a, b). 'Extra density' not accounted for by the partial model consisting of the pore, Fabs and voltage sensor paddles presumably contains the S1, S2 and S3a helices. This density is located mainly between the voltage sensor paddles from neighbouring subunits (red dashed ovals, Fig. 3c, d), not peripheral to the voltage sensor paddles. In several studies disulphide cross-links connecting S4 to the pore[16–18] have been given as evidence against S4 being located at the protein–lipid interface, but Fig. 3 suggests that such cross-links and a perimeter location for S4 are not mutually exclusive.

The electron microscopy map places an additional constraint on the S4 helix beyond the X-ray structures. In the two possible orientations of the paddle, the long straight S4 helix from the X-ray structure[4] of the isolated voltage sensor projects well beyond the surface (Fig. 4a, b), which implies that the helix must bend to fit the map. The red arrows (Fig. 4a, b) point to a glycine residue (Gly 134) where the S4 is bent in the full-length crystal structure of KvAP[4]; the correspondence of this glycine with the surface of the map implies that the S4 helix is also bent at this position in the single particle structure. In the KvAP crystal structure[4] the S4 was defined as the hydrophobic, arginine-containing helix amino-terminal to Gly 134, forming one helix of the voltage sensor paddle, whereas the S4–S5 linker was defined as the amphipathic helical segment running from Gly 134 to the N terminus of S5 (Fig. 4c). The map requires this

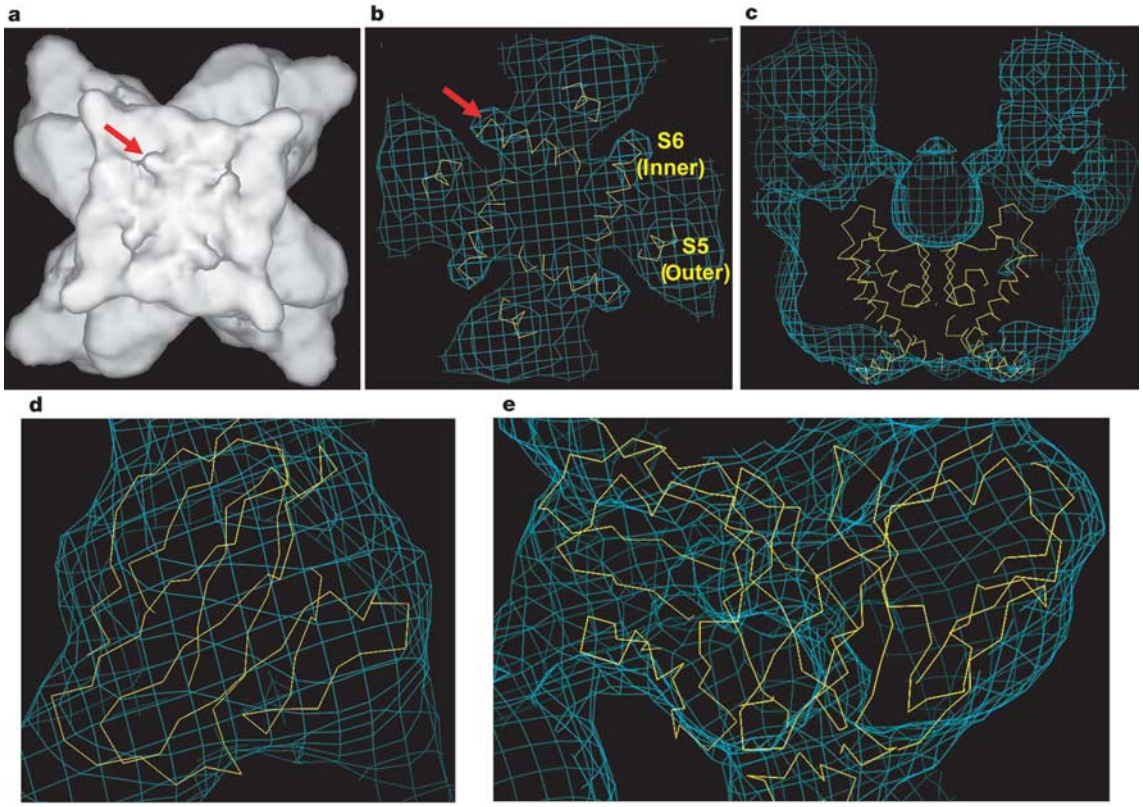

Figure 2 Docking of the crystal structures of the KvAP pore and 33H1Fab fragments into the electron microscope map. **a**, View of the map of the KvAP–33H1 complex from the intracellular side. The short tubes (red arrow) show α-helices projecting from the surface. **b**, Cross section near the intracellular surface of the map (blue mesh) with the KvAP pore (PDB code 1ORQ, yellow traces) in position. The ends of S6 correspond to the protruding tubes (red arrow). S5 projects into the density beside S6. **c**, Side-view of a central section of the map (blue mesh) with the docked pore (yellow trace). **d**, **e**, Docking of the variable immunoglobulin domain of the Fab (PDB code 1ORS, yellow trace) into the map (blue mesh). The view in **d** was identified by a red asterisk in Fig. 1e. The map in **e** was rotated 90° anti-clockwise along the vertical axis from the orientation in **d**.

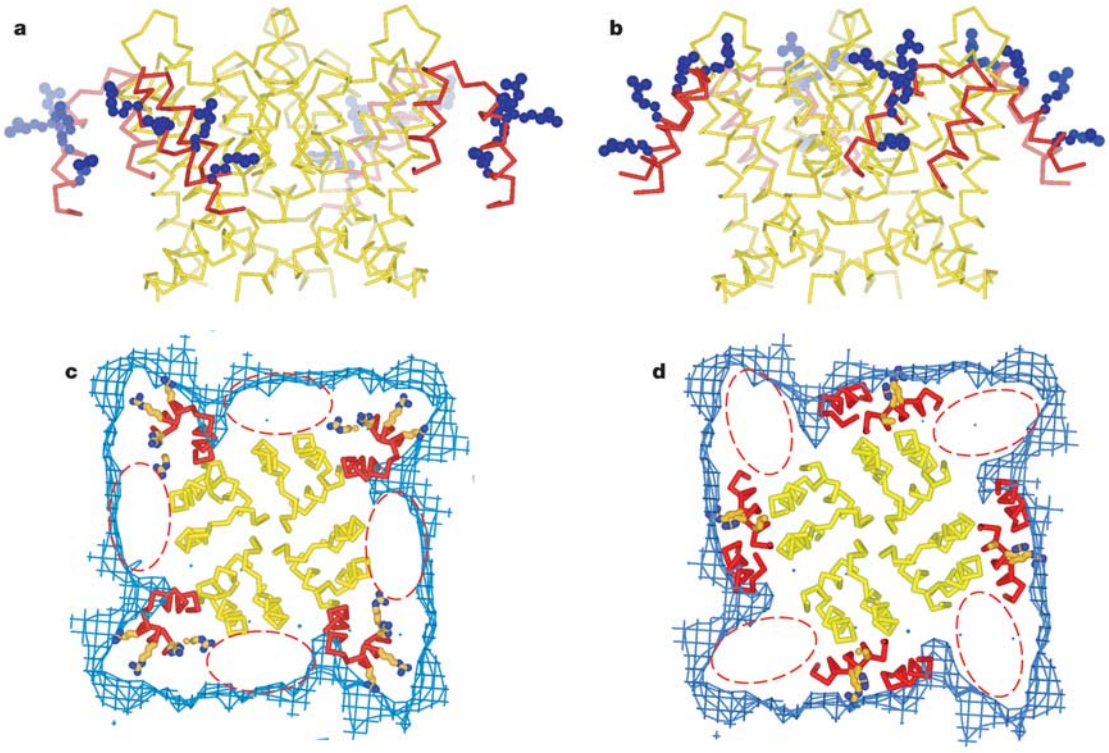

Figure 3 Two possible orientations of the paddle relative to the pore. **a**, **b**, Two orientations of the paddle (red) are shown beside the pore (yellow). Arginine residues on S4 are shown in blue. **c**, **d**, Cross sections of the map (blue mesh) at the extracellular surface with the paddle and the pore in position. The extra density (highlighted by red dashed ovals) could be accounted for by S1, S2 and S3a for each possible orientation of the paddle.

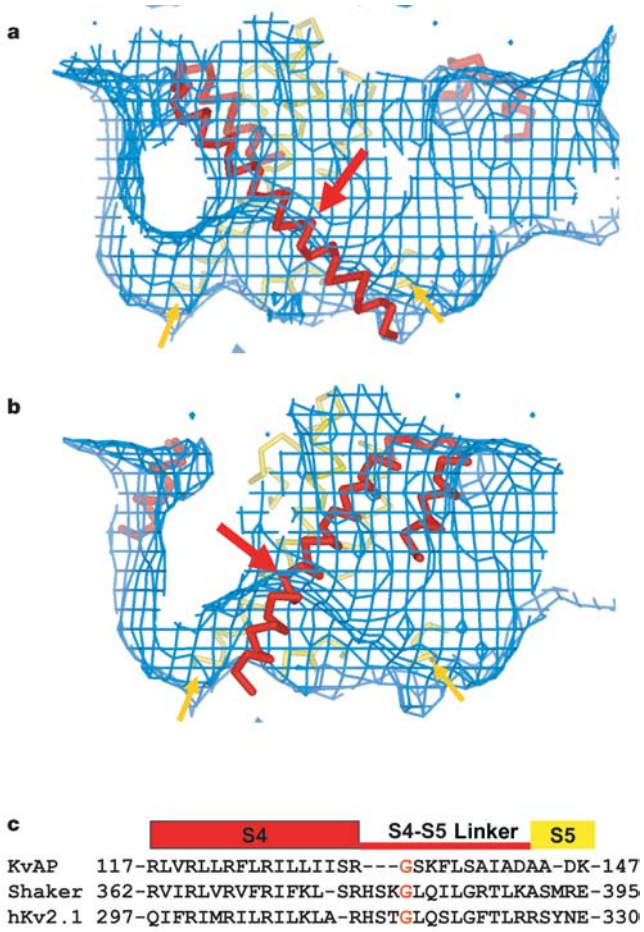

Figure 4 The S4 probably bends and becomes the S4–S5 linker at Gly 134. **a**, **b**, The long S4 helix (red helix) from the crystal structure of the isolated voltage sensor (PDB code 1ORS) projects beyond the map (blue mesh). In either possible orientation, Gly 134 (red arrow) is located near the surface of the map. The S4 is bent at this position in the crystal structure of full-length KvAP (PDB code 1ORQ). Yellow arrows show the locations of nearby S5 helices. **c**, Alignment of S4 and S4–S5 linker sequences of KvAP, *Shaker* and human Kv2.1 potassium channels. The linker sequence is not conserved, but has a distinct amphipathic feature with a glycine residue (highlighted in red) close to its beginning.

linker to run parallel to the membrane surface to reach a nearby S5 helix, although we can not tell from the map which adjacent S5 it is attached to (yellow arrows, Fig. 4a, b). This suggests that the S4 helix is only about five helical turns, not much longer than the length of the paddle, and that the S4–S5 linker (originally proposed to be part of S4 based on sequence alignments)[19] is interfacial near the intracellular solution. These assignments of S4 and linker are consistent with functional data showing that the first four arginine residues in the *Shaker* K^+ channel of *Drosophila* carry most of the gating charge[20,21].

The electron microscopy data give us a picture of a voltage-dependent K^+ channel with its voltage sensors in the membrane-depolarized, open conformation. In contrast to the crystal structure of KvAP in which the voltage sensor paddles adopted an intracellular position (but not a closed position)[4], the voltage sensor paddles in the single particles are 'up'. There are two very obvious and important aspects to the electron microscopy structure. First, the voltage sensor paddles are very near the extracellular solution. If one were to imagine a membrane surrounding the channel then the four highly conserved S4 arginine residues would be electrically near the extracellular solution. In other words, the gating charges would be displaced to their open channel positions. Second, the voltage sensor paddles are at the perimeter of the channel. This position of the paddles at the perimeter is not consistent with the conventional model in which S4 is hypothesized to rotate or translate within a protein-lined, aqueous gating pore[6,7]. It is consistent with the hypothesis that the voltage sensor moves at the protein–lipid interface when the channel undergoes a conformational change from the closed to open state[4,5]. □

Methods

Preparation of KvAP–33H1 complexes

The KvAP channel protein was expressed in XL1-blue strain *Escherichia coli* and purified as described previously[3]. The 33H1 Fab was prepared according to standard protocols[4]. Stable KvAP–33H1 complexes were purified on a Superdex 200 size-exclusion column. The protein was concentrated to about 5.0 mg ml^{-1} with a Millipore concentrator (100 kDa molecular weight cut off) in a buffer containing 5 mM n-Decyl-β-D-Maltopyranoside, 40 mM KCl, 60 mM NaCl and 20 mM Tris-HCl at pH 7.4.

Negative stain and cryo-negative stain electron microscopy

For negative staining, freshly carbon-coated copper grids were glow-discharged for 2 min immediately before use. The KvAP–33H1 complexes of 0.10 mg ml^{-1} were applied to the grid. After 1 min the solution was blotted almost completely away, to leave a thin layer of sample on the surface. The grid was then quickly floated on top of a drop of stain solution (6.0% ammonium molybdate-NaOH, pH 6.7–7.4 and 2.0% trehalose). After 10–15 s, the stain solution was completely blotted, and the grid was dried in a desiccator under vacuum for 3 h.

To prepare cryo-negative stain samples, holey grids were covered with a layer of thin carbon film (~15 nm) and glow-discharged for 2.0 min before use. Immediately before freezing, a saturated solution of ammonium molybdate (~65%, pH adjusted to 6.7–7.4 with 10.0 M NaOH) was prepared. Equal volumes of the stain solution and the protein sample (~5.0 mg ml^{-1}) were mixed and 3.0 μl of the mixture was applied to a holey grid. After about 10 s the grid was transferred to a guillotine plunger, blotted with a slip of filter paper, and immediately plunged into liquid ethane. The cryo-specimens were stored in liquid nitrogen until electron microscope examination.

The negative-stain specimens were examined in a Phillips CM12 microscope operated at 120 kV, and the cryo-negative stain specimens in either the CM12 or a Phillips CM200 FEG microscope run at 200 kV. The defocus range was −0.5 to −1.1 μm. The low-dose mode was used to take pictures using Kodak SO-163 films at × 60,000 magnification with the CM12 and × 50,000 magnification with the CM200. For cryo-negative stain specimens the electron dose was kept at ~20 e_0 per Å^2 per exposure.

Image analysis

Films were developed in full-strength D19 for 12 min. Images were examined on an optical diffractometer and only those with no obvious drift or astigmatism were digitized in a Zeiss SCAI scanner (ZI imaging) at 14 μm steps, corresponding to 2.8 Å on the specimen level with the CM200 microscope.

The analysis of the images followed standard protocols[22,23]. The defocus level for each electron micrograph was determined by CTF fitting using a MATLAB program (the Mathworks). The B factors estimated from the CTF fitting of the films were ~100 Å^2. Single particles were interactively selected from each image by use of the BOXER program in the EMAN package[24]. The particle images were extracted and then phase-flipped with the CTFIT in EMAN. The IMAGIC package[25] was used to generate two initial models by angular reconstitution[26] from a negative-stain data set (~4,500 particle images) and a cryo-negative stain data set (~8,200) collected in the CM12. The two models were at 28 Å and 19 Å resolution, respectively. Multivariate statistical analysis of both data sets showed strong four-fold symmetry, consistent with the channels being tetramers with four Fab fragments bound to each channel. These two models were taken as the references to process in the SPIDER package[27] a large data set of 28,960 particles picked from 36 micrographs taken in the CM200 FEG microscope. The two initial models gave rise to the same final map after the refinement. 90% of the particles were selected based on the correlation coefficient with the reference map. The final map was calculated from 21,379 particles after overpopulated classes were limited in size in the final reconstruction. For amplitude correction, a B factor of 100 Å^2 and an amplitude contrast constant of 15% (ref. 28) were used in the Wiener filtering[29], which had little effect on the map. Data assessing the accuracy with which the final map represents the particle images are presented in Supplementary Information. The resolution of the final map was estimated by applying the 0.5 threshold to the Fourier shell correlation[12,13] between two maps calculated from two halves of the data. The map was contoured at a density level to give ~340 kDa to the KvAP–Fab complex, taking into account about 40 kDa for the detergent micelle.

The docking of the crystal structures of the KvAP pore (protein data bank (PDB) code 1ORQ) and the Fab fragment–voltage sensor paddle (PDB code 1ORS) was performed manually using the program O (ref. 30).

Received 17 March; accepted 3 June 2004; doi:10.1038/nature02735.

1. Sigworth, F. Voltage gating of ion channels. *Q. Rev. Biophys.* **27,** 1–40 (1994).
2. Bezanilla, F. The voltage sensor in voltage-dependent ion channels. *Physiol. Rev.* **80,** 555–592 (2000).
3. Ruta, V., Jiang, Y., Lee, A., Chen, J. & MacKinnon, R. Functional analysis of an archaebacterial voltage-dependent K^+ channel. *Nature* **422,** 180–185 (2003).
4. Jiang, Y. *et al.* X-ray structure of a voltage-dependent K^+ channel. *Nature* **423,** 33–41 (2003).
5. Jiang, Y., Ruta, V., Chen, J., Lee, A. & MacKinnon, R. The principle of gating charge movement in a voltage-dependent K^+ channel. *Nature* **423,** 42–48 (2003).
6. Bezanilla, F. Voltage sensor movements. *J. Gen. Physiol.* **120,** 465–473 (2002).

7. Horn, R. Coupled movements in voltage-gated ion channels. *J. Gen. Physiol.* **120,** 449–453 (2002).
8. Frank, J. Single-particle imaging of macromolecules by cryo-electron microscopy. *Annu. Rev. Biophys. Biomol. Struct.* **31,** 303–319 (2002).
9. Henderson, R. The potential and limitations of neutrons, electrons and X-rays for atomic resolution microscopy of unstained biological molecules. *Q. Rev. Biophys.* **28,** 171–193 (1995).
10. Adrian, M., Dubochet, J., Fuller, S. D. & Harris, J. R. Cryo-negative staining. *Micron* **29,** 145–160 (1998).
11. Golas, M. M., Sander, B., Will, C. L., Luhrmann, R. & Stark, H. Molecular architecture of the multiprotein splicing factor SF3b. *Science* **300,** 980–984 (2003).
12. Saxton, W. O. & Baumeister, W. The correlation averaging of a regularly arranged bacterial cell envelope protein. *J. Microsc.* **127,** 127–138 (1982).
13. van Heel, M. Similarity measures between images. *Ultramicroscopy* **21,** 95–100 (1987).
14. Conway, J. F. *et al.* Characterization of a conformational epitope on hepatitis B virus core antigen and quasiequivalent variations in antibody binding. *J. Virol.* **77,** 6466–6473 (2003).
15. Rosenthal, P. B. & Henderson, R. Optimal determination of particle orientation, absolute hand, and contrast loss in single-particle electron cryomicroscopy. *J. Mol. Biol.* **333,** 721–745 (2003).
16. Laine, M. *et al.* Atomic proximity between S4 segment and pore domain in *Shaker* potassium channels. *Neuron* **39,** 467–481 (2003).
17. Gandhi, C. S., Clark, E., Loots, E., Pralle, A. & Isacoff, E. Y. The orientation and molecular movement of a K^+ channel voltage-sensing domain. *Neuron* **40,** 515–525 (2003).
18. Neale, E. J., Elliott, D. J., Hunter, M. & Sivaprasadarao, A. Evidence for intersubunit interactions between S4 and S5 transmembrane segments of the *Shaker* potassium channel. *J. Biol. Chem.* **278,** 29079–29085 (2003).
19. Chandy, K. G. & Gutman, G. A. in *Ligand and Voltage-Gated Channels* (ed. North, R. A.) 1–72 (CRC, Boca Raton, 1995).
20. Seoh, S. A., Sigg, D., Papazian, D. M. & Bezanilla, F. Voltage-sensing residues in the S2 and S4 segments of the *Shaker* K^+ channel. *Neuron* **16,** 1159–1167 (1996).
21. Aggarwal, S. K. & MacKinnon, R. Contribution of the S4 segment to gating charge in the *Shaker* K^+ channel. *Neuron* **16,** 1169–1177 (1996).
22. Orlova, E. V. *et al.* Structure of keyhole limpet hemocyanin type 1 (KLH1) at 15 Å resolution by electron cryomicroscopy and angular reconstitution. *J. Mol. Biol.* **271,** 417–437 (1997).
23. Gabashvili, I. S. *et al.* Solution structure of the *E. coli* 70S ribosome at 11.5 Å resolution. *Cell* **100,** 537–549 (2000).
24. Ludtke, S. J., Baldwin, P. R. & Chiu, W. EMAN: semiautomated software for high-resolution single-particle reconstructions. *J. Struct. Biol.* **128,** 82–97 (1999).
25. van Heel, M., Harauz, G., Orlova, E. V., Schmidt, R. & Schatz, M. A new generation of the IMAGIC image processing system. *J. Struct. Biol.* **116,** 17–24 (1996).
26. van Heel, M. Angular reconstitution: a posteriori assignment of projection directions for 3D reconstruction. *Ultramicroscopy* **21,** 111–123 (1987).
27. Frank, J. *et al.* SPIDER and WEB: processing and visualization of images in 3D electron microscopy and related fields. *J. Struct. Biol.* **116,** 190–199 (1996).
28. Sander, B., Golas, M. M. & Stark, H. Automatic CTF correction for single particles based upon multivariate statistical analysis of individual power spectra. *J. Struct. Biol.* **142,** 392–401 (2003).
29. Hawkes, P. W. in *Computer Processing of Electron Microscopic Images* (ed. Hawkes, P. W.) 1–33 (Springer, Berlin, 1980).
30. Jones, T. A., Zou, J. Y., Cowan, S. W. & Kjeldgaard Improved methods for building protein models in electron density maps and the location of errors in these models. *Acta Crystallogr. A* **47,** 110–119 (1991).

Supplementary Information accompanies the paper on **www.nature.com/nature**.

Acknowledgements We thank members of the MacKinnon lab, S. Darst, N. Opalka and D. Stokes for helpful discussions. This work was supported by grants from the NIH to D.N.W. and R.M. R.M is an investigator in the Howard Hughes Medical Institute.

Competing interests statement The authors declare that they have no competing financial interests.

Correspondence and requests for materials should be addressed to R.M. (mackinn@rockefeller.edu). The electron microscopy map has been deposited with European Bioinformatics Institute (www.ebi.ac.uk/msd/emd-2771.map).

corrigenda

Enzymic activation and transfer of fatty acids and acyl-adenylates in mycobacteria

Omita A. Trivedi, Pooja Arora, Vijayalakshmi Sridharan, Rashmi Tickoo, Debasisa Mohanty & Rajesh S. Gokhale

Nature **428,** 441–445 (2004).

The structures of lauroyl–AMP and lauroyl–CoA are incorrectly represented in Fig. 1c, d of this Letter, which shows the L-form rather than the natural D-form of adenosine; there is no phosphate group at the 2′-position of the ribosyl moiety of lauroyl–AMP (Fig. 1c) and the phosphate group in lauroyl–CoA (Fig. 1d) should be at the 3′-position. These errors do not affect our conclusions. □

Reduction of hysteresis losses in the magnetic refrigerant $Gd_5Ge_2Si_2$ by the addition of iron

Virgil Provenzano, Alexander J. Shapiro & Robert D. Shull

Nature **429,** 853–857 (2004).

It has come to our attention that we failed to cite in our Letter to *Nature* a key publication[1] that describes changes in the magnetocaloric capabilities of $Gd_5(Si_2Ge_2)$ as a result of alloying the compound with small amounts of various metals, including iron. That paper supports the findings presented in our Letter. However, we also show that it is important to consider the magnetic hysteresis in addition to the magnetocaloric effect when assessing the usefulness of a material as a magnetic refrigerant. □

1. Pecharsky, V. K. & Gschneidner, K. A. Effect of alloying on the giant magnetocaloric effect of $Gd_5(Si_2Ge_2)$. *J. Magn. Magn. Mater. Res.* **167,** L179–L184 (1997).